

Article

Improving Transverse Compressive Modulus of Carbon Fibers during Wet Spinning of Polyacrylonitrile

Sherman Wong ^{1,*} , Linda K. Hillbrick ², Jasjeet Kaur ², Aaron J. Seeber ¹, Jurg A. Schutz ² 
and Anthony P. Pierlot ²

¹ CSIRO Manufacturing, Clayton, VIC 3168, Australia; aaron.seeber@csiro.au

² CSIRO Manufacturing, Waurn Ponds, VIC 3216, Australia; linda.hillbrick@gmail.com (L.K.H.); jasjeet.kaur17@yahoo.com (J.K.); jurg.schutz@csiro.au (J.A.S.); tpierlot@bigpond.com (A.P.P.)

* Correspondence: sherman.wong@csiro.au

Abstract: The performance of carbon fibers depends on the properties of the precursor polyacrylonitrile (PAN) fibers. Stretching of PAN fibers results in improved tensile properties, while potentially reducing its compressive properties. To determine optimization trade-offs, the effect of coagulation conditions and the stretching process on the compressive modulus in the transverse direction (E_T) was investigated. A method for accurately determining E_T from polymer fibers with non-circular cross-sectional shapes is presented. X-ray diffraction was used to measure the crystallite size, crystallinity, and crystallite orientation of the fibers. E_T was found to increase with decreasing crystallite orientation along the drawing direction, which decreases the tensile modulus in the longitudinal direction (E_L) proportionally to crystallite orientation. Stretching resulted in greater crystallite orientation along the drawing direction for fibers formed under the same coagulation conditions. Increasing the solvent concentration in the coagulation bath resulted in a higher average orientation, but reduced the impact of stretching on the orientation. The relationship between E_T and E_L observed in the precursor PAN fiber is retained after carbonization, with a 20% increase in E_T achieved for a 2% decrease in E_L . This indicates that controlled stretching of PAN fiber allows for highly efficient trading off of E_L for E_T in carbon fiber.

Keywords: fiber compression; microstructure of fibers; structure–property relations



Citation: Wong, S.; Hillbrick, L.K.; Kaur, J.; Seeber, A.J.; Schutz, J.A.; Pierlot, A.P. Improving Transverse Compressive Modulus of Carbon Fibers during Wet Spinning of Polyacrylonitrile. *Fibers* **2022**, *10*, 54. <https://doi.org/10.3390/fib10060054>

Academic Editor: Sushanta Ghoshal

Received: 22 April 2022

Accepted: 10 June 2022

Published: 14 June 2022

Publisher's Note: MDPI stays neutral with regard to jurisdictional claims in published maps and institutional affiliations.



Copyright: © 2022 by the authors. Licensee MDPI, Basel, Switzerland. This article is an open access article distributed under the terms and conditions of the Creative Commons Attribution (CC BY) license (<https://creativecommons.org/licenses/by/4.0/>).

1. Introduction

Carbon fiber (CF) is an important modern construction material due to its light weight and high tensile properties. This has made CF-reinforced composites an ideal construction material for the aerospace and wind energy industries [1–3]. The properties of the composite are highly dependent on the properties of the individual [4,5]. Thus, there is considerable interest in measuring and modifying the mechanical properties of individual CFs. The most widely used method for producing CFs is by carbonization of a polyacrylonitrile (PAN) fiber precursor, commonly called a white fiber (WF). The WF spinning process is a crucial step in the production of CF, as the structural properties of the final CF will be determined by the structure of the WF [6–9]. Thus, the processing parameters of the WF have been the focus of much study [10–12].

A high-quality WF with strong tensile properties requires a strong orientation along the fiber axis, high crystallinity, minimal voids, and a circular cross-section [13,14]. Drawing the fiber during the coagulation process (i.e., jet stretch) and after coagulation (i.e., post-draw stretch) are important processing conditions for tailoring these properties. The total increase in length between the extruded fiber and the final WF is known as the total draw ratio (TDR). Increasing the TDR during the spinning process increases the orientation along the fiber axis [15], increases the crystallinity [16] and the homogeneity [17], and promotes the formation of a rounded cross-section [18]. Surface roughness also increases

with drawing [19,20], which must be accounted for when considering its properties in the transverse direction. A well-drawn fiber results in superior tensile properties, such as increased tensile strength and tensile modulus [13,15,18,21,22].

However, there has been minimal reported consideration on the impact of TDR on the CF compressive properties, despite the fact that most carbon fiber reinforced materials are limited not by their tensile properties but by their compression properties in practical applications [4,23,24]. A potential reason for the relative paucity of compression studies compared to tension studies of CFs and their precursor WFs is the added complexity of measuring the compressive properties of a single fiber.

Different methods have been reported in the literature to address this. Firstly, traditional nanoindentation experiments have been supported with mathematical models, atomic force microscopy, and finite element analysis to ensure the unconstrained circular cross-section of the fiber does not impact the result [25,26]. Another method probes CFs embedded in a composite using nanoindentation to measure the reduced modulus in the transverse and longitudinal directions from which the five unique stiffness coefficients of a transversely isotropic fiber can then be calculated [27–30]. In the method used here, the free-standing fiber is compressed and a Hertzian contact mechanics model is used to account for the circular cross-sectional shape of the fiber. This technique has been applied both to CF [31–33] and to polymer fibers [34,35].

While some modifications due to increasing TDR are expected to also improve compressive properties (e.g., reduction of voids, high crystallinity), orientation of the graphitic crystallites along the fiber axis are expected to negatively impact the compressive properties. Most prominently, the orientation of graphitic sheets such that their planes are layered perpendicular to the compression direction will reduce the compressive modulus.

Here, WFs processed under different spinning conditions and TDRs were compressed along the transverse direction to measure transverse compressive modulus (E_T), which was compared to its longitudinal tensile modulus (E_L) and the orientation of the crystallites. Furthermore, several WFs were carbonized, and the moduli of the CF were also compared. While increasing E_T resulted in a decreased E_L , a significant increase in E_T was observed for minimal decrease in E_L . This promising result suggests that E_T can be tailored to the required application by varying the TDR during WF spinning, maximizing the compressive properties without meaningfully impacting the highly desirable tensile properties of CF.

2. Materials and Methods

2.1. Spinning

Two sets of WFs were spun using a wet-spinning technique on a 500-filament pilot-scale spinning line. The polymer solution consisted of commercially available polymer purchased from Japan Exlan Co., Ltd. (Osaka, Japan), which contains acrylonitrile, methyl acrylate, and itaconic acid in a 96:3:1 ratio, in a DMSO solvent with a polymer concentration of 20 wt % and a viscosity average molecular weight of 176 kg mol⁻¹. Using a discovery HR3 hybrid rheometer with parallel plates 40 mm apart, a flow sweep test at 70 °C and 1 s⁻¹ shear rate was performed to measure the polymer solution shear viscosity as 103 Pa.s. All fibers were extruded at a velocity of 2.50 m/min from a spinneret with a hole diameter of 80 µm. For the first set, the polymer was extruded into a 30 °C DMSO/water coagulation bath with a 70/30 vol % ratio and a residence time of 30 s, followed by a 40 °C DMSO/water gradient bath with a 50/50 vol % ratio with a residence time of 14 s. For the second set, the polymer was extruded into a single higher temperature 60 °C DMSO/water coagulation bath with a 65/35 vol % ratio, with a residence time of 30 s.

Both coagulation conditions had a jet stretch ratio of 0.7×. Thermal post drawing was subsequently performed on the same line, which involved a washing bath stretch, a hot water stretch, and a steam stretch. For the WF extruded into a 30 °C coagulation bath (hereafter, “30C series”) a wash bath stretch of 1.25×, a hot water stretch of 2.50×, and a variable steam stretch for a total draw ratio of 7.2×, 8.0×, 9.2×, 10.0×, and 10.8× was applied. For the WF extruded into a 60 °C coagulation bath (hereafter, “60C series”) a

wash bath stretch of 1.62×, a hot water stretch of 2.50×, and a variable steam stretch for a total draw ratio of 7.8×, 10.0×, and 12.6× was applied. These parameters were chosen as they were found to minimize pores and filament breakage. The processing parameters for each sample are listed in Table 1, with the assigned name based on their coagulation bath temperatures (i.e., 30 °C and 60 °C) and their TDR. For example, the 30C series WF that has a TDR of 9.2 is named 30C-9×.

Table 1. The coagulation bath conditions, the stretching ratios at each stretching stage, and the total draw ratio (TDR) of the WFs measured in this study.

Name	Coagulation Conditions	Jet Stretch	Wash Bath Stretch	Hot Water Stretch	Steam Stretch	TDR
30C-7×	70% DMSO @ 30 °C + 50% DMSO @ 40 °C	0.7	1.25	2.50	3.29	7.2
30C-8×	70% DMSO @ 30 °C + 50% DMSO @ 40 °C	0.7	1.25	2.50	3.66	8.0
30C-9×	70% DMSO @ 30 °C + 50% DMSO @ 40 °C	0.7	1.25	2.50	4.20	9.2
30C-10×	70% DMSO @ 30 °C + 50% DMSO @ 40 °C	0.7	1.25	2.50	4.57	10.0
30C-11×	70% DMSO @ 30 °C + 50% DMSO @ 40 °C	0.7	1.25	2.50	4.94	10.8
60C-8×	65% DMSO @ 60 °C	0.7	1.62	2.50	2.76	7.8
60C-10×	65% DMSO @ 60 °C	0.7	1.62	2.50	3.51	10.0
60C-13×	65% DMSO @ 60 °C	0.7	1.62	2.50	4.44	12.6

2.2. Carbonization

Select WFs (60C-8×, 60C-10×, 60C-13×) were carbonized on the carbon fiber production line at Carbon Nexus, Deakin University (Australia). All three WFs were drawn through four oxidation zones with a tension of 100 cN across a single 500-filament tow, at temperatures of 230, 240, 250, and 260 °C for Zones 1 through 4, respectively. This was followed by drawing with a tension of 50 cN, through low temperature carbonization zones at temperatures of 450, 550, and 650 °C through Zones 1 to 3, respectively. Finally, the fiber was drawn with a tension of 100 cN through high temperature carbonization zones at a temperature of 1100 and 1400 °C for Zones 1 and 2, respectively. The line speed was 22 m/h, resulting in a dwell time within each zone of 16.4, 4.9, and 3.2 min in the oxidation zones, low temperature carbonization zones, and high temperature carbonization zones, respectively. Both low- and high-temperature carbonization zones were filled with nitrogen to create an inert atmosphere.

2.3. Compression

The compression was performed on the fiber compression instrument detailed in [36], using the analysis method included therein. In particular, the removal of the ‘initial section’ removes the impact of surface roughness that is introduced by increased drawing. E_T was fitted to the Hertzian contact mechanics model developed by Morris et al. [37]

$$U = \frac{4F}{\pi} \left(\frac{1}{E_T} \right) \left(\sinh^{-1} \left(\frac{R}{b} \right) \right) \quad (1)$$

where F is the force per unit length, R is the radius of the fiber, and b is the contact segment width between the fiber and the tip. This model was chosen based on a comparative study of the available models by Hillbrick et al. [38].

All fibers (i.e., both WF and CF samples) were compressed at a rate of 1 μm/s using 0.1 μm steps up to the maximum load, held at maximum load for either 120 s (first compression of a fiber) or 5 s (subsequent compressions on the same fiber, at a different location), and then released at the same rate. The longer hold duration was used to analyze the non-elastic deformation (detailed in Figure 1 and the associated text) of the fiber, with the outcome of this analysis inferred for the subsequent 5 s hold duration compressions on the fiber. The presented E_T values were fitted from the loading segments of both, 120 s and 5 s hold compressions, with no measurable difference between 120 s and 5 s observed. The WFs were compressed to a maximum load of ~50 mN over 10 s, while the CFs were

compressed up to a maximum load of ~500 mN over 100 s. Several (5–10) compressions were performed at different positions along each individual fiber, and at least 4 individual fibers were tested for each sample type.

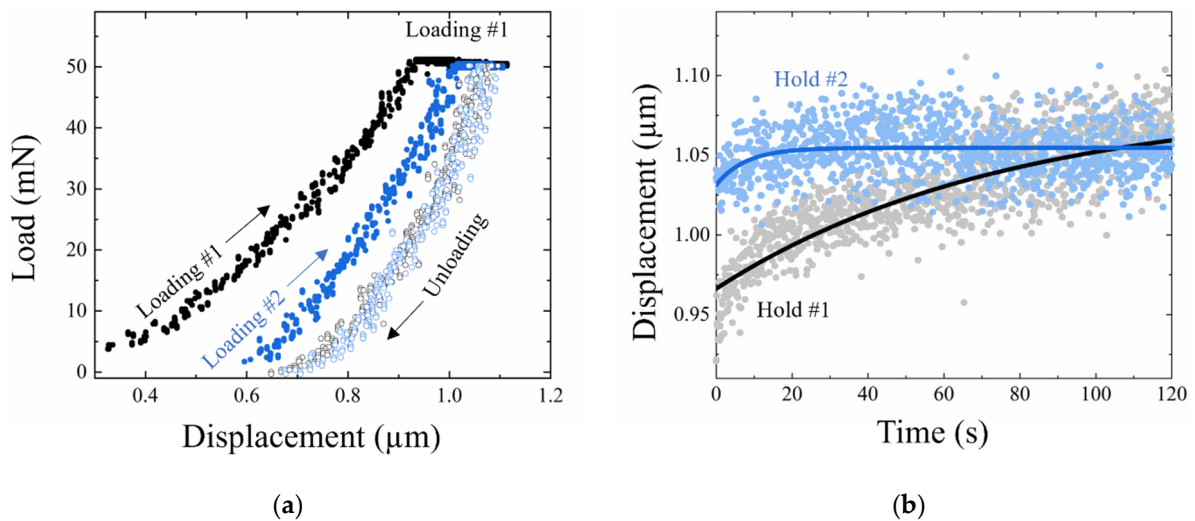


Figure 1. (a) Load–displacement curves from sequential compression of 30C-7× WF at the same position (first—Black; second—Blue). Each cycle consists of a loading segment (solid circle), a 120 s hold segment at maximum load (solid circle), and an unloading segment (empty circle). (b) Creep during the hold segment, showing the exponential decay to the point creep plateaus. The data (solid circles) have been fitted with an exponential decay function (line).

The compression displacement of the CFs remained constant during the hold duration; however, the compression displacement of the WFs increased during the hold duration due to polymer creep [39]. This creep was also present within the loading curve, and was dependent upon the loading rate and the amount of physical aging undergone by the polymer [40,41], which changes the fitted E_T . Thus, the physical aging of the WF samples were standardized by heating them above their glass transition (T_g) followed by controlled cooling to reset the amount of aging experienced. Each sample was heated at 120 °C for 1 h, then cooled at a rate of no greater than 10 °C/h and compressed 20 days after cooling.

2.4. SEM

SEM images of the fiber cross-sections were obtained using a Hitachi TM4000 under an accelerating voltage of 5 kV. WFs were prepared for SEM imaging by securing a 500-filament tow using rubber tubing, freezing the sample in liquid nitrogen, and then cutting using a microtome to minimize the impact on the cross-sectional shape. The fibers were not coated. The SEM images were used to determine R for the WF samples.

2.5. Favimat

Tensile testing was performed using a Textechno H. Stein Favimat + Robot 2 single fiber tester equipped with single-fiber clamps to measure E_L and breaking stress for all fibers. The testing was performed on fibers of gauge length 25 mm, with a pretension of 1 cN/tex and a testing speed of 10 mm/min. For the WF fibers, 25 fibers were tested; while 50 fibers were tested for the CF samples, and the average value was taken. Favimat testing was also used to determine the cross-sectional area for the CF samples, from which a value for R was calculated.

2.6. X-ray Diffraction (XRD)

XRD was performed using a Rigaku SmartLab diffractometer equipped with a Cu $K\alpha$ source. To measure the crystallinity and crystal size, parallel beam scanning in transmission mode was performed across the range $2\theta = 5^\circ$ – 60° . The profile was fitted using TOPAS-

Academic, Version 6 (Coelho Software), with peaks fitted using a pseudo-Voigt function. The crystallinity was determined using

$$\text{Crystallinity} = \frac{A_C}{A_A + A_C} \quad (2)$$

where A_C is the summed area of the first and second order (001) crystalline peaks at $\sim 17^\circ$ and $\sim 29^\circ$ and A_A is the area of the amorphous peak at $\sim 26^\circ$ [42,43]. The crystallite size was determined using Scherrer's equation:

$$\text{Crystallite Size} = \frac{K\lambda}{\beta \cos\theta} \quad (3)$$

where K is the Scherrer constant (0.89 in this case), λ is the wavelength (1.541 Å for Cu $K\alpha$), and β is the FWHM of the peak at $\sim 17^\circ$. To measure orientation, a 2D image was taken and integrated azimuthally over the peak at $\sim 17^\circ$. This integrated profile was fitted using a Lorentzian function, with the orientation defined as:

$$\text{orientation} = \frac{180 - \varepsilon}{180} \quad (4)$$

where ε is the FWHM of the integrated profile. Under this definition, a theoretical perfectly aligned sample would have an orientation of 1. Due to instrumental broadening, the practical maximum is most likely in the 0.95–1 region.

3. Results and Discussion

3.1. Subsection

A number of issues need to be considered when analyzing a transverse compression displacement curve on a (viscoelastic) polymeric fiber, such as physical ageing, creep, and plastic (permanent) deformation. Figure 1a presents two load–displacement curves from the same position on the same 30C-7× WF, one directly after the other. In both compressions, the sample was held under maximum load for 120 s, during which time the displacement increased (i.e., polymer creep). The decay of the creep rate is plotted in Figure 1b, showing the creep plateaus during the hold segment. The presence of creep impacts the determination of E_T by fitting the elastic portion of the loading curve in two ways. Firstly, creep will be present throughout the loading curve, making it viscoelastic, hence the need to compare fibers with identical loading rates. This issue was addressed by keeping the strain rate the same between all WF compressions performed. Secondly, the presence of creep masks the presence of plasticity. That is, for an elastic material, the loading and unloading curves will overlap when the sample remains within its elastic regime. For a viscoelastic material, the loading and unloading curves never overlap; therefore, it is not readily apparent if the loading curve has entered the plastic regime and contains a section unsuitable for calculating E_T .

To identify if permanent, plastic deformation has occurred, two loading and unloading experiments were performed sequentially in the same fiber position with a hold period at maximum load and the two unloading curves compared. The first loading curve (Figure 1a) shows the displacement with increasing load, with contributions due to creep. During the first hold duration at maximum load, the amount of creep plateaus. For the first unloading and second loading curves, much of the creep remains present, making these sections unsuitable for fitting. During the second hold duration, the sample returns quickly to the creep plateau. Finally, the second unloading overlaps with the first unloading curve as they share essentially identical starting positions. If the sample had responded plastically, or if the creep had not plateaued after the first hold duration, the two unloading curves would not overlap. Thus, we suggest that an overlapping pair of unloading curves is evidence that plasticity has not occurred and that the first loading curve can be fitted to provide an accurate E_T value.

Figure 2a shows two loading curves from a single 30C-7 \times fiber at positions less than 2 mm apart, with the fitted curve and E_T values indicated. The considerable difference between these two curves and their fitted E_T was typical for 30C-7 \times WF, resulting in a mean $E_T = 1.96$ (0.52) GPa (value in brackets are standard deviations) across 95 different compressions and a coefficient of variation (CoV) of 27%. A histogram plotting all measured E_T values is shown in Figure 2b. The values appear to be from a bimodal distribution rather than a single distribution. The higher and lower distributions give a mean $E_{T,higher} = 2.29$ (0.26) GPa and $E_{T,lower} = 1.37$ (0.25) GPa resulting in a $CoV_{higher} = 11\%$ and $CoV_{lower} = 18\%$, respectively. This double distribution is observed even when comparing data taken from a single fiber, indicating it is not due to differences between individual fibers.

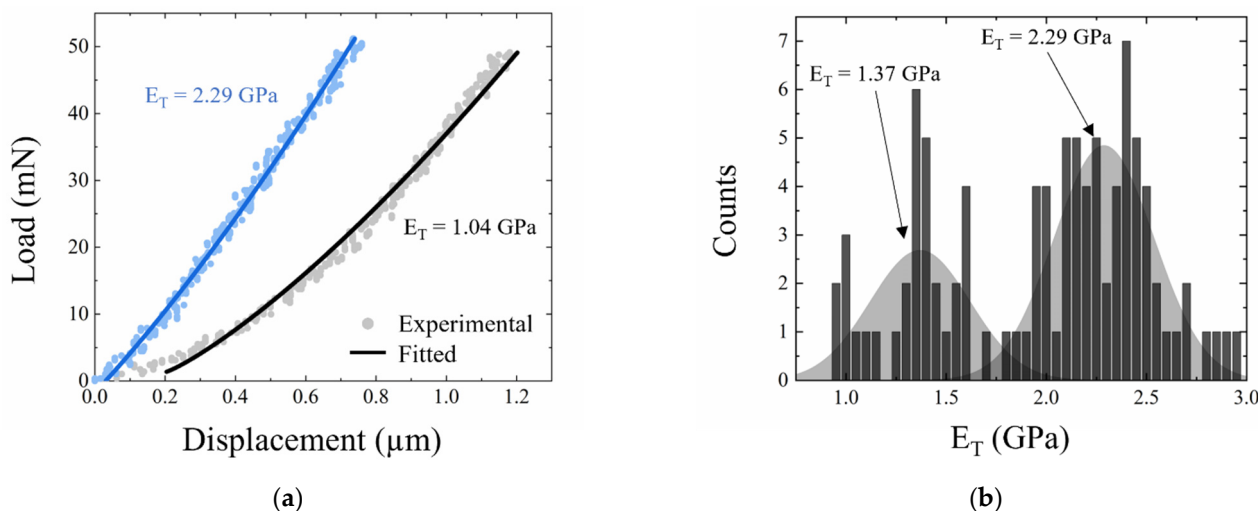


Figure 2. (a) Two fitted load–displacement curves from 30C-7 \times WF, with E_T as indicated. These compressions were performed on the same fiber, with compression position less than 2 mm apart. (b) A histogram showing the distribution of the fitted E_T values. The data is best fit by two normal distributions, centered at 1.37 GPa and 2.29 GPa with a standard deviation of 0.25 GPa and 0.26 GPa, respectively.

Figure 3a presents an SEM image of 30C-7 \times WF cross-sections, showing that some of the cross-sections are circular, while others are bean-shaped. As the analysis method used to fit E_T depends on the cross-sections being (roughly) circular, we propose that the higher distribution is due to erroneously applying the method to bean-shaped cross-sections which are much closer to rectangular in shape. Indeed, refitting the curves that comprise the higher distribution using a standard $E = \text{stress}/\text{strain}$ relationship results in $E_T = 1.36$ (0.30) GPa, which is consistent with $E_{T,lower} = 1.32$ (0.21) GPa. Figure 3b–e shows that circular and bean-shaped cross-sections were observed in all other WFs in the 30C series, and a similar double distribution was also observed in E_T values fitted from the load–displacement curves. The remainder of this study discarded the $E_{T,higher}$ values and considered $E_T = E_{T,lower}$ for these five WF types.

Increasing the coagulation bath temperature is reported to promote the formation of WFs with cross-sections that are circular [44,45]. SEM images of the 60C series are presented in Figure 4, where the cross-sections are almost all circular. Fitting the compression data for these WFs resulted in a single distribution, supporting the proposal that the double distribution is due to the mixture of bean-shaped and circular cross-sections found in the 30C series of WFs. The E_T values for all WFs are compiled in Table 2 alongside the tensile properties measured using the Favimat, E_L and breaking stress.

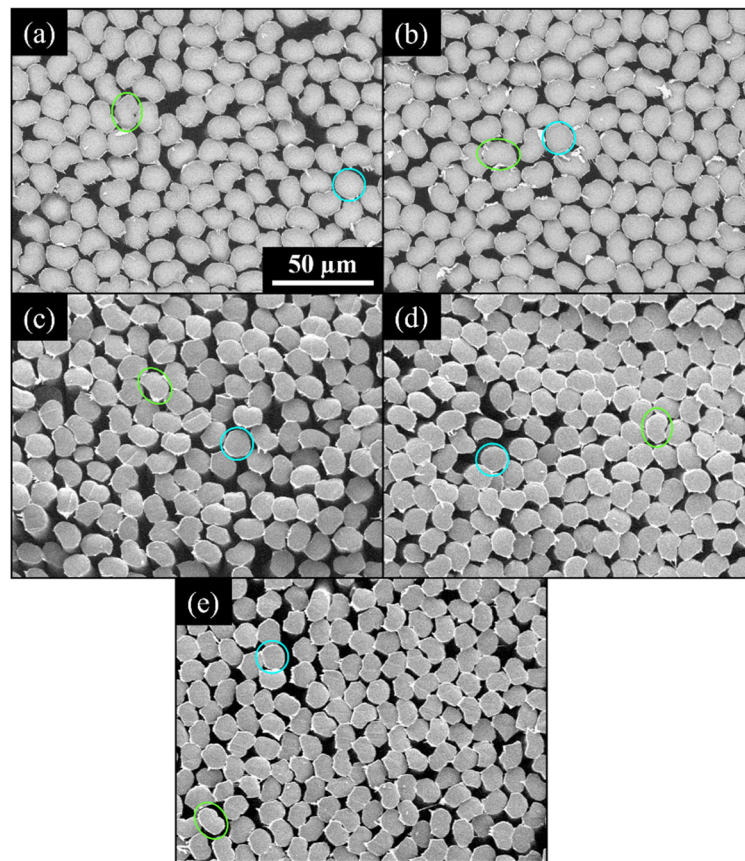


Figure 3. SEM images showing the cross-sectional shape for (a) 30C-7 \times , (b) 30C-8 \times , (c) 30C-9 \times , (d) 30C-10 \times , and (e) 30C-11 \times . All images are at the same scale. An example of a circular (blue) and bean-shaped (green) cross-section has been indicated.

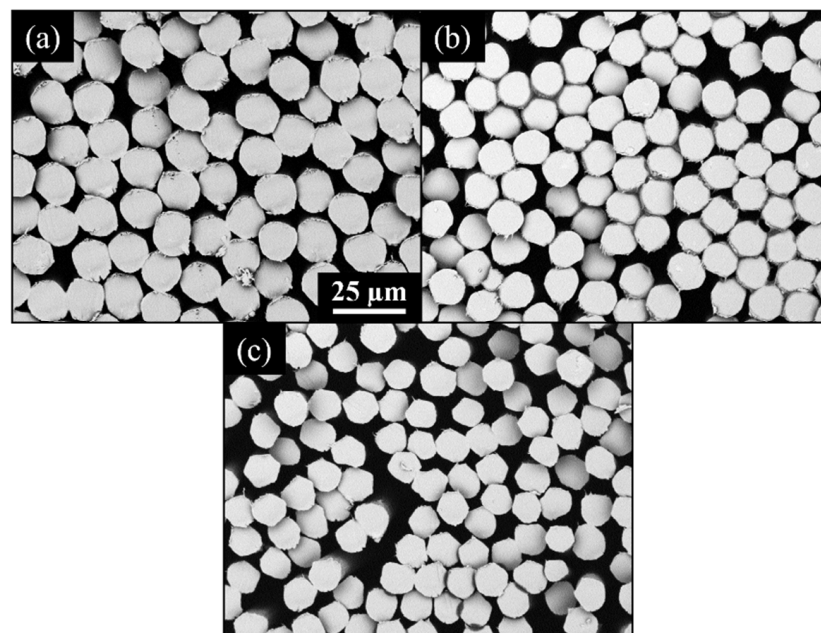


Figure 4. SEM images showing the cross-sectional shape for (a) 60C-8 \times , (b) 60C-10 \times , and (c) 60C-13 \times . All images are at the same scale.

Table 2. The mean E_L values, the breaking stress, the mean E_T values, and the densities for the WFs and CFs investigated in this study. The E_L and density values were measured using a Favimat. Standard deviations are indicated in the round brackets. The confidence intervals (95% confidence) have been provided for the modulus values. The number of measurements is indicated after each confidence interval in curly brackets.

Name	E_L (GPa)	Con. Int. 95%	Breaking Stress (GPa)	E_T (GPa)	Con. Int. 95%	Density (g/cm ³)
30C-7×	16.6 (0.28)	0.12 {25}	0.89 (0.05)	1.32 (0.21)	0.08 {32}	0.67 (0.09)
30C-8×	16.8 (0.33)	0.14 {23}	0.90 (0.08)	1.10 (0.20)	0.07 {34}	1.18 (0.08)
30C-9×	17.6 (0.24)	0.10 {25}	1.00 (0.06)	1.24 (0.27)	0.07 {62}	1.18 (0.06)
30C-10×	17.9 (0.34)	0.14 {24}	1.07 (0.06)	0.93 (0.11)	0.08 {10}	1.18 (0.11)
30C-11×	18.3 (0.29)	0.12 {25}	1.09 (0.07)	1.06 (0.19)	0.08 {24}	1.18 (0.10)
60C-8×	15.5 (0.32)	0.13 {25}	0.79 (0.05)	1.63 (0.20)	0.09 {20}	1.18 (0.06)
60C-10×	16.9 (0.32)	0.13 {25}	0.81 (0.06)	1.65 (0.14)	0.06 {20}	1.18 (0.08)
60C-13×	18.0 (0.37)	0.15 {25}	0.94 (0.09)	1.22 (0.16)	0.07 {20}	1.18 (0.07)

Figure 5a plots the relationship between E_T and E_L for the WFs investigated, with the error bars representing standard deviation. Overall, there appears to be a linearly decaying relationship between E_T and E_L . However, the relationship between TDR and E_T is not straightforward, as shown in Figure 5b. While there is no general trend between the two series, there appears to be a trend within each series of WFs. This suggests that the coagulation conditions also have a significant impact on how the TDR can impact the E_T .

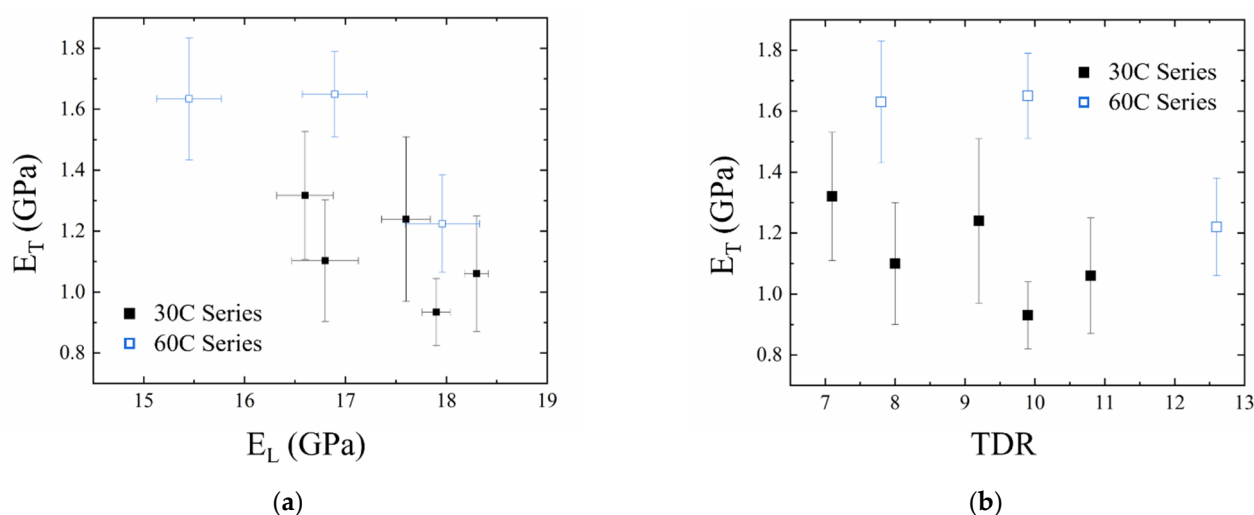


Figure 5. Plots showing the dependence of E_T on (a) E_L and (b) TDR for the WFs measured in this study. The error bars represent the standard deviation.

3.2. XRD

To explore this further, the orientation, crystallite size, and crystallinity of the WFs were measured using XRD, with the results presented in Table 3. Figure 6a shows a typical 2D diffraction image from the WF and the azimuthally integrated profile centered at $2\theta = 17^\circ$ as indicated by the dashed line. The FWHM (ϵ) of this peak is used to calculate the crystallite orientation of the WFs. Figure 6b shows that more stretching increased the orientation for both series, but in a different manner. A linear fit for both series is presented in Figure 6b. For the 30C series there is a slope of 1.8×10^{-3} which intercepts TDR = 10 at 0.955. For the 60C series, there is a slope of 3.3×10^{-3} which intercepts TDR = 10 at 0.935. That is, the 30C series has a higher average value but increases at a lower rate with respect to TDR. Figure 6c shows that more stretching increased the crystallite size in a linear manner, with both series following the same trend. Figure 6d shows that the crystallinity did not appear to be dependent on the TDR within the range investigated. It is important to note that while the crystallinity has generally been reported to increase with increased stretching in the

literature [16,18,46], such studies are on a single WF as it is increasingly stretched during its spinning process. Here, multiple finished WFs experiencing different spinning conditions are being compared. Bajaj et al. compared finished WF with $4\times$, $5\times$, and $6\times$ TDR and saw no increase in the crystallinity with respect to stretching [47]. However, they also observed no change in crystallinity throughout the entire spinning process. Shin et al. reported that the stage at which stretching is applied (i.e., jets stretch or post-draw stretch) has a significantly larger impact on crystallinity than the TDR [48]. Moskowitz et al. compared WFs with constant TDR distributed differently between the initial jet stretch and the final post-draw stretch [49]. They observed a decrease in crystallinity as the WF progressed along the spinning process despite the additional stretching, but the finished WF had the same crystallinity for all samples. They concluded that crystallinity is difficult to measure and interpret due to the convolution of the amorphous and second order peaks. That is to say, the crystallinity of WFs is impacted by many spinning parameters and does not necessarily share a linear relationship with any parameter, including post-draw stretching. The most probable proposal is that, within our coagulation conditions, there is a maximum crystallinity of $\sim 75\%$ which has been reached by all WFs studied.

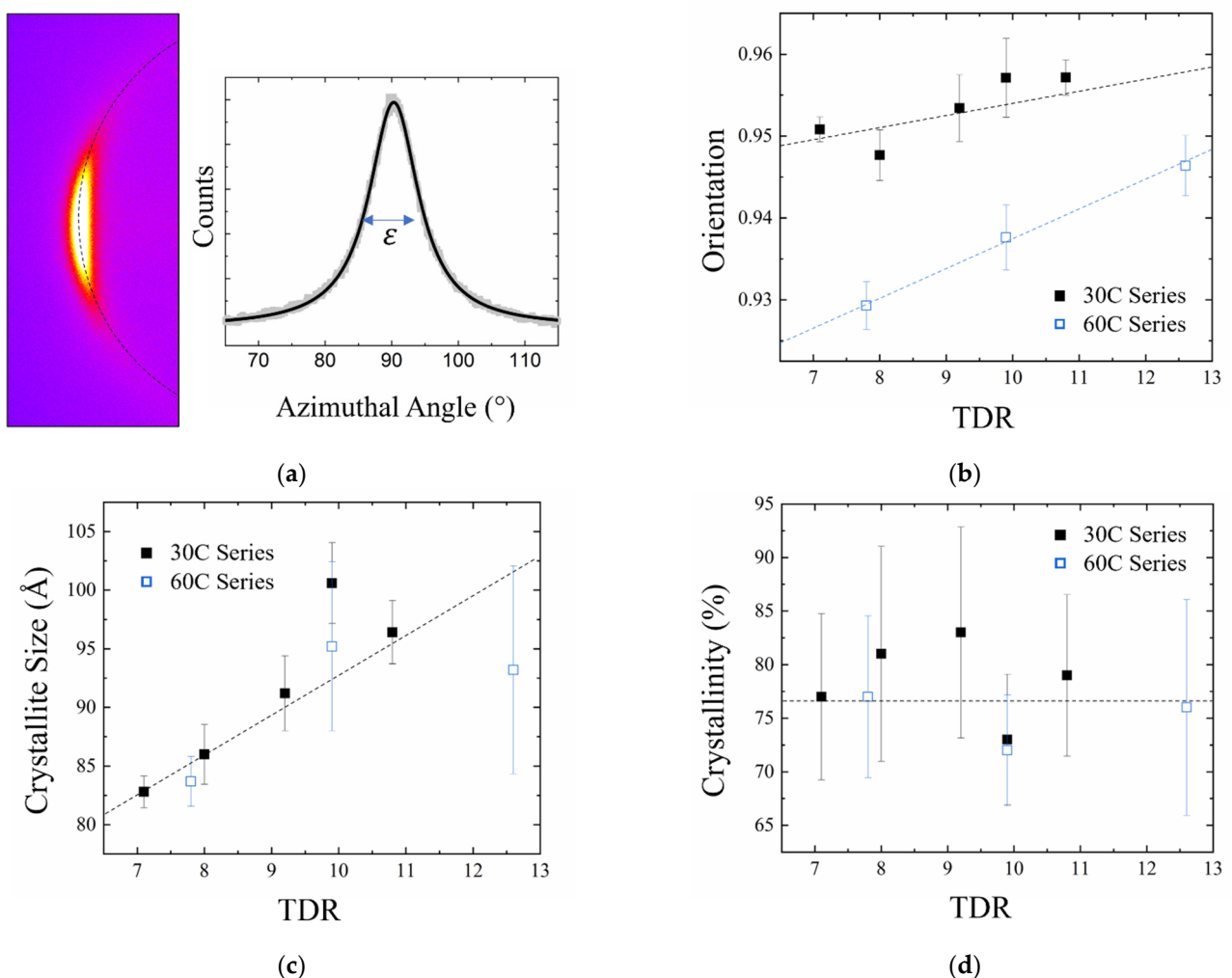


Figure 6. (a) A typical 2D diffraction pattern from a WF (left) and the peak profile resulting from azimuthally integrating along the ring indicated by the dashed line (right). Relationship between TDR and (b) orientation, (c) crystallite size, and (d) crystallinity for the WFs measured in this study. The error bars represent (a,b) the standard deviation and (c,d) the experimental uncertainty.

Table 3. The orientation, crystallinity, and the crystallite size as measured using XRD for the WFs investigated in this study. Standard deviations are indicated in the round brackets, while experimental error is indicated after the \pm sign.

Name	Orientation	Crystallinity (%)	Crystallite Size (Å)
30C-7 \times	0.955 (0.004)	77 \pm 8	83 \pm 1
30C-8 \times	0.952 (0.005)	81 \pm 10	86 \pm 3
30C-9 \times	0.949 (0.004)	83 \pm 10	91 \pm 10
30C-10 \times	0.962 (0.004)	73 \pm 6	101 \pm 4
30C-11 \times	0.960 (0.004)	79 \pm 8	96 \pm 8
60C-8 \times	0.929 (0.005)	77 \pm 8	84 \pm 2
60C-10 \times	0.938 (0.004)	72 \pm 5	95 \pm 7
60C-13 \times	0.946 (0.004)	76 \pm 10	92 \pm 13

The key difference between the crystal structures of the 30C and 60C series is the orientation, with the 30C series having a higher overall orientation, but the increase in orientation with increasing TDR is lower. The higher overall orientation can be attributed to the effect of spinning conditions excluding post-draw stretching on the orientation. WFs have been reported to have orientation at the point of coagulation, before any post-draw stretching has been applied, which affects the orientation of the finished WF [18,21]. Furthermore, some WFs are more readily aligned in the direction of drawing [50]. In particular, a higher solvent concentration in the coagulation bath results in higher orientation for WFs of similar TDR [8], consistent with the observation here that the 30C series with higher DMSO concentration has a higher orientation. Regarding the decreased impact of stretching for the 30C series, stretching to increase orientation has diminishing returns as the sample approaches the maximum practical orientation given instrumental limitations.

Therefore, the relationship between TDR and orientation is only applicable to WF produced under similar coagulation conditions. Rather, when E_T is plotted against orientation—as shown in Figure 7—an inversely proportional relationship is observed, confirming that orientation is correlated to E_T . These results highlight the importance of the coagulation conditions, which determines the impact of subsequent stretching on the crystal structure and mechanical properties of the WF. Therefore, the solvent concentration must also be considered when modifying the orientation to engineer more desirable mechanical properties.

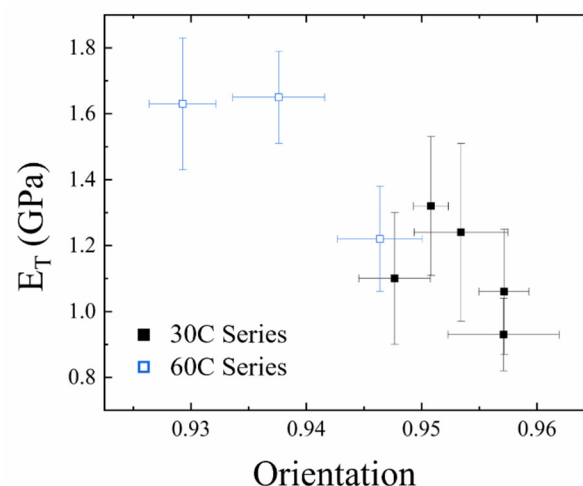


Figure 7. Relationship between E_T and orientation for the WFs measured in this study. The error bars represent the standard deviation.

3.3. Carbonization

To confirm the inverse relationships between E_T and E_L are preserved in the final CF, the 60C series WFs were carbonized. Figure 8 plots E_T to E_L for the 60C series after carbonization, with the error bars representing (a) standard deviation and (b) confidence

intervals with 95% confidence level. The standard deviation describes the distribution of E_T measurements (including physical variance within the fiber structure) and does not reflect the uncertainty in the mean result, whereas the confidence interval clearly shows that the inverse relationship between E_T and E_L and its dependence on stretching has remained after carbonization. The difference between the E_T gained to the E_L lost is significant, with a 20% increase in E_T to a 2% decrease in E_L .

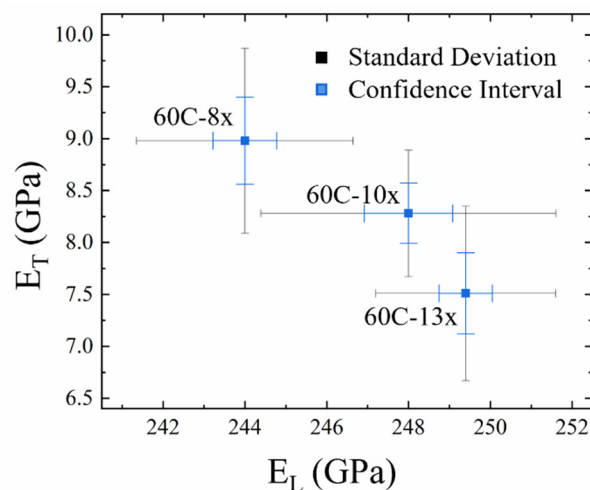


Figure 8. Relationship between E_T and E_L for the CFs measured in this study. The error bars represent the standard deviation (black) and 95% confidence intervals (blue).

4. Conclusions

Compression was performed on WFs that were formed under two sets of coagulation conditions, with increasing amounts of post drawing applied to the WFs within each set, to investigate the relationship between the TDR and E_T . To fit E_T from a compression curve, a loading segment that did not exhibit plastic deformation behavior was fitted using the elastic contact mechanics model developed by Morris et al. Due to the presence of polymer creep, it was not readily apparent whether plasticity had occurred during compression. Instead, a method for determining if the offset is from polymer creep or plastic deformation is presented. In this method, the WF is allowed to creep until a plateau is reached, unloaded, and then immediately recompressed. The unloading curves of these two compressions will overlap if no plastic deformation has occurred.

SEM imaging suggested the cross-sectional shape of the WF had a significant impact on the fitted E_T value, with bean-shaped cross-sections fitting a much higher E_T . Thus, only WFs with a circular cross-section were considered. As expected, the E_T increased when the orientation of the crystallites within the WF decreased, which also resulted in a slight decrease in E_L . For WFs with similar TDR, a higher solvent concentration in the coagulation bath resulted in a higher orientation. However, it also resulted in less sensitivity to changes in the TDR. Thus, while reducing the amount of post drawing is a powerful method for increasing the E_T of a WF, consideration of the coagulation conditions prior to post-draw stretching is required to fully utilize this method. Further studies could be done by lowering the coagulation bath solvent concentration and TDR to explore the amount E_T can be improved before other desirable properties of the WF (and resultant CF) become significantly impacted.

For the WFs where reduced stretching resulted in reduced orientation, the increase in E_T remained after carbonization. This resulted in a CF that had a 20% increase in E_T with negligible loss of E_L . This not only suggests that E_L can be systematically traded for increased E_T by controlled stretching, but it also suggests that this can be done in a highly efficient manner to maximize E_T gained in the final CF.

Author Contributions: Conceptualization, S.W., A.J.S., L.K.H., J.K. and A.P.P.; Methodology, S.W., J.A.S. and J.K.; Validation, S.W., L.K.H. and J.K.; Formal analysis, S.W. and J.A.S.; Investigation, S.W. and J.A.S.; Resources, L.K.H., J.K., A.J.S., J.A.S. and A.P.P.; Data curation, S.W. and A.J.S.; Writing—original draft preparation, S.W., A.J.S. and A.P.P.; Writing—review and editing, All authors; Visualization, S.W. and A.P.P.; Supervision, A.P.P.; Project administration, S.W. and A.P.P. All authors have read and agreed to the published version of the manuscript.

Funding: This research received no external funding.

Institutional Review Board Statement: Not applicable.

Informed Consent Statement: Not applicable.

Data Availability Statement: The data presented in this study are openly available in FigShare at <https://doi.org/10.6084/m9.figshare.19624311> (accessed on 21 April 2022).

Acknowledgments: The authors would like to acknowledge Nicole Phair-Sorenson and Debra Hamilton for performing the Favimat testing and SEM imaging, respectively.

Conflicts of Interest: The authors declare that they have no known competing financial interests or personal relationships that could have appeared to influence the work reported in this paper.

References

1. Fitzer, E. Pan-based carbon fibers—present state and trend of the technology from the viewpoint of possibilities and limits to influence and to control the fiber properties by the process parameters. *Carbon* **1989**, *27*, 621–645. [CrossRef]
2. Krenkel, W.; Berndt, F. C/C–SiC composites for space applications and advanced friction systems. *Mater. Sci. Eng. A* **2005**, *412*, 177–181. [CrossRef]
3. Khayyam, H.; Fakhrhoseini, S.M.; Church, J.S.; Milani, A.S.; Bab-Hadiashar, A.; Jazar, R.N.; Naebe, M. Predictive modelling and optimization of carbon fiber mechanical properties through high temperature furnace. *Appl. Therm. Eng.* **2017**, *125*, 1539–1554. [CrossRef]
4. Kumar, I.P.; Mohite, P.; Kamle, S. Axial compressive strength testing of single carbon fibres. *Arch. Mech.* **2013**, *65*, 27–43.
5. Ji, X.; Wang, C.; Francis, B.A.; Chia, E.S.; Zheng, L.; Yang, J.; Joshi, S.C.; Chen, Z. Mechanical and interfacial properties characterisation of single carbon fibres for composite applications. *Exp. Mech.* **2015**, *55*, 1057–1065. [CrossRef]
6. Barnet, F.R.; Norr, M.K. A three-dimensional structural model for a high modulus pan-based carbon fibre. *Composites* **1976**, *7*, 93–99. [CrossRef]
7. Chari, S.S.; Bahl, O.P.; Mathur, R.B. Characterisation of acrylic fibres used for making carbon fibres. *Fibre Sci. Technol.* **1981**, *15*, 153–160. [CrossRef]
8. Morris, E.A.; Weisenberger, M.C.; Rice, G.W. Properties of PAN Fibers Solution Spun into a Chilled Coagulation Bath at High Solvent Compositions. *Fibers* **2015**, *3*, 560–574. [CrossRef]
9. Lee, J.-E.; Chae, Y.K.; Lee, D.J.; Choi, J.; Chae, H.G.; Kim, T.H.; Lee, S. Microstructural evolution of polyacrylonitrile fibers during industry-mimicking continuous stabilization. *Carbon* **2022**, *195*, 165–173. [CrossRef]
10. Han, C.D.; Segal, L. A study of fiber extrusion in wet spinning. II. Effects of spinning conditions on fiber formation. *J. Appl. Polym. Sci.* **1970**, *14*, 2999–3019. [CrossRef]
11. Kulichikhin, V.G.; Skvortsov, I.Y.; Mironova, M.I.; Ozerin, A.N.; Kurkin, T.S.; Berkovich, A.K.; Frenkin, E.I.; Malkin, A.Y. From Polyacrylonitrile, its Solutions, and Filaments to Carbon Fibers II. Spinning PAN-Precursors and their Thermal Treatment. *Adv. Polym. Technol.* **2018**, *37*, 1099–1113. [CrossRef]
12. Sun, L.; Shang, L.; Xiao, L.; Zhang, M.; Li, M.; Ao, Y. Structural changes of polyacrylonitrile fibers in the process of wet spinning. *J. Appl. Polym. Sci.* **2020**, *137*, 48905. [CrossRef]
13. Kaur, J.; Millington, K.; Smith, S. Producing high-quality precursor polymer and fibers to achieve theoretical strength in carbon fibers: A review. *J. Appl. Polym. Sci.* **2016**, *133*, 43963. [CrossRef]
14. Ahn, H.; Yeo, S.Y.; Lee, B.-S. Designing Materials and Processes for Strong Polyacrylonitrile Precursor Fibers. *Polymers* **2021**, *13*, 2863. [CrossRef] [PubMed]
15. Sen, K.; Bajaj, P.; Sreekumar, T.V. Thermal behavior of drawn acrylic fibers. *J. Polym. Sci. Part B-Polym. Phys.* **2003**, *41*, 2949–2958. [CrossRef]
16. Kirsten, M.; Meinel, J.; Schonfeld, K.; Michaelis, A.; Cherif, C. Characteristics of wet-spun and thermally treated poly acrylonitrile fibers. *J. Appl. Polym. Sci.* **2016**, *133*, 9. [CrossRef]
17. Gao, Q.; Jing, M.; Chen, M.; Zhao, S.; Wang, Y.; Qin, J.; Yu, M.; Wang, C. Force field in coagulation bath at low temperature induced microfibril evolution within PAN nascent fiber and precursor fiber. *J. Appl. Polym. Sci.* **2020**, *137*, 49380. [CrossRef]
18. Wang, Y.X.; Wang, C.G.; Bai, Y.J.; Bo, Z. Effect of the drawing process on the wet spinning of polyacrylonitrile fibers in a system of dimethyl sulfoxide and water. *J. Appl. Polym. Sci.* **2007**, *104*, 1026–1037. [CrossRef]

19. Gao, Q.; Jing, M.; Chen, M.; Zhao, S.; Wang, W.; Qin, J.; Wang, C. Microfibril alignment induced by stretching fields during the dry-jet wet spinning process: Reinforcement on polyacrylonitrile fiber mechanical properties. *Polym. Test.* **2020**, *81*, 106191. [[CrossRef](#)]
20. Wang, Y.; Tong, Y.; Zhang, B.; Su, H.; Xu, L. Formation of Surface Morphology in Polyacrylonitrile (PAN) Fibers during Wet-Spinning. *J. Eng. Fibers Fabr.* **2018**, *13*, 52–57. [[CrossRef](#)]
21. Ouyang, Q.; Chen, Y.; Wang, X.; Ma, H.; Li, D.; Yang, J. Supramolecular structure of highly oriented wet-spun polyacrylonitrile fibers used in the preparation of high-performance carbon fibers. *J. Polym. Res.* **2015**, *22*, 229. [[CrossRef](#)]
22. Gao, Q.; Jing, M.; Wang, C.; Zhao, S.; Chen, M.; Qin, J. Preparation of high-quality polyacrylonitrile precursors for carbon fibers through a high drawing ratio in the coagulation bath during a dry-jet wet spinning process. *J. Macromol. Sci. Part B* **2019**, *58*, 128–140. [[CrossRef](#)]
23. Oya, N.; Johnson, D.J. Longitudinal compressive behaviour and microstructure of PAN-based carbon fibres. *Carbon* **2001**, *39*, 635–645. [[CrossRef](#)]
24. Chand, S. Review carbon fibers for composites. *J. Mater. Sci.* **2000**, *35*, 1303–1313. [[CrossRef](#)]
25. Li, H.; Liu, C.; Chen, J. Predicting and Characterizing Plastic Deformation Behavior of Transversely-isotropic Carbon Fiber Monofilament Using Finite Element Simulation and Nanoindentation. *Fibers Polym.* **2021**, *22*, 2316–2322. [[CrossRef](#)]
26. Duan, S.; Liu, F.; Pettersson, T.; Creighton, C.; Asp, L.E. Determination of transverse and shear moduli of single carbon fibres. *Carbon* **2020**, *158*, 772–782. [[CrossRef](#)]
27. Csanádi, T.; Németh, D.; Zhang, C.; Dusza, J. Nanoindentation derived elastic constants of carbon fibres and their nanostructural based predictions. *Carbon* **2017**, *119*, 314–325. [[CrossRef](#)]
28. Tane, M.; Okuda, H.; Tanaka, F. Nanocomposite microstructures dominating anisotropic elastic modulus in carbon fibers. *Acta Mater.* **2019**, *166*, 75–84. [[CrossRef](#)]
29. Shirasu, K.; Nagai, C.; Naito, K. Mechanical anisotropy of PAN-based and pitch-based carbon fibers. *Mech. Eng. J.* **2020**, *7*, 19–00599. [[CrossRef](#)]
30. Shirasu, K.; Goto, K.; Naito, K. Microstructure-elastic property relationships in carbon fibers: A nanoindentation study. *Compos. Part B Eng.* **2020**, *200*, 108342. [[CrossRef](#)]
31. Kawabata, S. Measurement of the transverse mechanical-properties of high-performance fibers. *J. Text. Inst.* **1990**, *81*, 432–447. [[CrossRef](#)]
32. Fujita, K.; Sawada, Y.; Nakanishi, Y. Effect of cross-sectional textures on transverse compressive properties of pitch-based carbon fibers. *J. Soc. Mater. Sci. Jpn.* **2001**, *50*, 116–121. [[CrossRef](#)]
33. Naito, K.; Tanaka, Y.; Yang, J.-M. Transverse compressive properties of polyacrylonitrile (PAN)-based and pitch-based single carbon fibers. *Carbon* **2017**, *118*, 168–183. [[CrossRef](#)]
34. Guo, Z.; Chen, W.; Zheng, J. Improved quasi-static twin-fiber transverse compression of several high-performance fibers. *Text. Res. J.* **2019**, *89*, 1595–1613. [[CrossRef](#)]
35. Sockalingam, S.; Bremble, R.; Gillespie, J.W., Jr.; Keefe, M. Transverse compression behavior of Kevlar KM2 single fiber. *Compos. Part A Appl. Sci. Manuf.* **2016**, *81*, 271–281. [[CrossRef](#)]
36. Wong, S.; Pierlot, A.; Abbott, A.; Schutz, J. Direct Measurement of the Transverse Modulus of Carbon Fibres. *Exp. Mech.* **2022**, *62*, 769–778. [[CrossRef](#)]
37. Morris, S. The Determination of the Lateral-Compression Modulus of Fibres. *J. Text. Inst.* **1968**, *59*, 536–547. [[CrossRef](#)]
38. Hillbrick, L.K.; Kaiser, J.; Huson, M.G.; Naylor, G.R.S.; Wise, E.S.; Miller, A.D.; Lucas, S. Determination of the transverse modulus of cylindrical samples by compression between two parallel flat plates. *SN Appl. Sci.* **2019**, *1*, 724–738. [[CrossRef](#)]
39. Raghavan, J.; Meshii, M. Creep rupture of polymer composites. *Compos. Sci. Technol.* **1997**, *57*, 375–388. [[CrossRef](#)]
40. Struik, L.C.E. *Physical Aging in Amorphous Polymers and Other Materials*; Elsevier Scientific Pub. Co.: Amsterdam, The Netherlands, 1977.
41. Nguyen-Tri, P.; Ghassemi, P.; Carriere, P.; Nanda, S.; Assadi, A.A.; Nguyen, D.D. Recent applications of advanced atomic force microscopy in polymer science: A review. *Polymers* **2020**, *12*, 1142. [[CrossRef](#)]
42. Bohn, C.; Schaeffgen, J.; Statton, W.J. Laterally ordered polymers: Polyacrylonitrile and poly (vinyl trifluoroacetate). *Polym. Sci* **1961**, *55*, 531. [[CrossRef](#)]
43. Ge, Y.; Fu, Z.; Deng, Y.; Zhang, M.; Zhang, H. The effects of chemical reaction on the microstructure and mechanical properties of polyacrylonitrile (PAN) precursor fibers. *J. Mater. Sci.* **2019**, *54*, 12592–12604. [[CrossRef](#)]
44. Knudsen, J.P. The influence of coagulation variables on the structure and physical properties of an acrylic fiber. *Text. Res. J.* **1963**, *33*, 13. [[CrossRef](#)]
45. Khayyam, H.; Jazar, R.N.; Nunna, S.; Golkarnarenji, G.; Badii, K.; Fakhrohoseini, S.M.; Kumar, S.; Naebe, M. PAN precursor fabrication, applications and thermal stabilization process in carbon fiber production: Experimental and mathematical modelling. *Prog. Mater. Sci.* **2020**, *107*, 100575. [[CrossRef](#)]
46. Gao, Q.; Jing, M.; Zhao, S.; Wang, Y.; Qin, J.; Yu, M.; Wang, C. Effect of spinning speed on microstructures and mechanical properties of polyacrylonitrile fibers and carbon fibers. *Ceram. Int.* **2020**, *46*, 23059–23066. [[CrossRef](#)]
47. Bajaj, P.; Sreekumar, T.V.; Sen, K. Structure development during dry-jet-wet spinning of acrylonitrile/vinyl acids and acrylonitrile/methyl acrylate copolymers. *J. Appl. Polym. Sci.* **2002**, *86*, 773–787. [[CrossRef](#)]

48. Shin, K.-A.; Park, S.; Nguyen, H.T.B.; Lee, J.H.; Lee, S.; Joh, H.-I.; Jo, S.M. Investigation into the gelation of polyacrylonitrile solution induced by dry-jet in spinning process and its effects on diffusional process in coagulation and structural properties of carbon fibers. *Macromol. Res.* **2018**, *26*, 544–551. [[CrossRef](#)]
49. Moskowitz, J.D.; Jackson, M.B.; Tucker, A.; Cook, J.D. Evolution of polyacrylonitrile precursor fibers and the effect of stretch profile in wet spinning. *J. Appl. Polym. Sci.* **2021**, *138*, 50967. [[CrossRef](#)]
50. Tan, L.; Liu, S.; Song, K.; Chen, H.; Pan, D. Gel-spun polyacrylonitrile fiber from pregelled spinning solution. *Polym. Eng. Sci.* **2010**, *50*, 1290–1294. [[CrossRef](#)]